Alteration of Hawaiian basalts under sulfur-rich conditions: Applications to understanding surface-atmosphere interactions on Mars and Venus

Molly C. McCanta[1,*], M. Darby Dyar[2], and Allan H. Treiman[3]

[1]Department of Earth and Ocean Sciences, Tufts University, Medford, MA 02155

[2]Department of Astronomy, Mount Holyoke College, 50 College St., South Hadley, MA 01075

[3]Lunar and Planetary Institute, 3600 Bay Area Blvd., Houston, TX 77058

Keywords: sulfate, Halemaumau, basalt weathering, Mössbauer spectroscopy, Mars, Venus

REVISION 1 – Correction date 9/8/2013

ABSTRACT

A suite of Hawaiian basalts that were variably altered in the presence of SO_2-rich gases during the current summit eruptive episode at Halemaumau crater, Kilauea, were studied to determine their alteration phase assemblage and reactive pathways using electron microscopy, Mössbauer spectroscopy, and X-ray diffraction. The alteration conditions represent an acid fog environment. Alteration rinds on the basalts vary in thickness from 10s of microns to the entirety of the rock and are composed of amorphous silica rims (85-95 wt.% SiO_2) overlain by sulfates. Sulfate mineralogy consisted of gypsum, anhydrite, and natroalunite-jarosite. No phyllosilicates were observed in any alteration assemblages. Phenocrysts and glass were both observed to be extensively reacted during alteration. The Halemaumau samples may provide good analogues for basalt alteration on other rocky planetary bodies, i.e., Mars, Venus, Mercury, where S is ubiquitous and low fluid/rock ratios are common.

INTRODUCTION

Both direct measurements and compositions inferred from meteorites and remote spectroscopy suggest that the terrestrial planets normally contain ~1-4% S by weight (e.g., Nittler et al., 2011), with varying mineralogical and geological hosts. Light elements like S are important constituents of both surface rocks and minerals and of planetary cores, where S lowers the melting temperature of pure Fe metal. In our solar system, the history of sulfur distribution can be traced through studies of primitive and evolved meteorites (Ebel, 2011) representing all stages of planetary accretion from impacts through differentiation to volcanism and subduction.

The motivation for this study lies in this ubiquitous occurrence of sulfur-bearing phases in surface rocks on terrestrial bodies and the types of processes, both alteration-driven and depositional, required to form them. For example, on the highly-reduced planet Mercury with its Fe-poor surface, large quantities of sulfur would be soluble in silicate melts, providing a driving force for explosive volcanism (e.g., Blewett et al 2011). The lack of an atmosphere on Mercury makes it likely that sulfides persist globally, as seen by workers such as Weider et al. (2012) who have mapped the ratio of S/Si across much of Mercury's northern hemisphere. Nittler et al. (2011) reported up to 4 wt.%, sulfur on the surface of Mercury based on MESSENGER results, postulated to occur in the form of Mg and Ca-rich sulfides based on x-ray spectrometry. This value is much higher than what is observed in differentiated asteroids, Martian meteorites, the Moon, or bulk Earth, suggesting that Mercury never underwent the depletion in volatile elements experienced by these other bodies (Peplowski et al. 2011). So the high sulfur distribution on Mercury's surface is a primary characteristic, and likely results from the enrichment of sulfur into silicate melts under reducing conditions (Nittler et al., 2011).

By way of contrast, the sulfur cycle on Venus is controlled by secondary interactions between the basaltic surface and the S-rich atmosphere (Zolotov 2007, Fegley and Prinn 1989). Few constraints on the elemental composition and mineralogy of the surface and subsurface exist, though they are critically needed to test models of surface evolution and weathering based on understanding of the physics and chemistry of Venus' crust and atmosphere. Three sets of XRF major element analyses from the Venera and Vega landers all suggest the presence of basaltic rock types along with variable amounts of sulfur, either primary or secondary from atmospheric interactions. Modeling based on these results by various workers (e.g., Zolotov et al. 1997, Treiman and Schwenzer 2009; Treiman and Bullock 2012) has provided the ground-

work and experimental context for distinguishing the contributions of chemical weathering reactions in an attempt to see through the geochemical overprinting to infer primary igneous rock compositions and mineralogy. The key to understanding Venus geology is to work backwards from the elemental and mineralogical compositions of surface-altered rocks to understand both the weathering products (and from them, rock-atmosphere interactions) and the rock type(s) from which they form.

The sulfur cycle on Mars is likely dominated by aqueous processes. Many direct chemical analyses of sulfur on Mars are available: 3.1±0.5 wt.% in dust and soil as measured by the Viking landers (Clark et al. 1982); 0.3- 2.7% S reported by Mars Pathfinder (Brückner et al. 2003), and 4.9-6.6% SO_3 (2.65% S) measured by the Mars Exploration Rovers (Rieder et al. 2004; Gellert et al. 2006) and the Mars Science Laboratory (Yen et al. 2013). A Mars global average surface sulfur abundance of 1.76 wt.% (4.40 wt.% SO_3) was reported based on Odyssey gamma-ray spectrometer (GRS) integrated observations (McLennan et al. 2010), reflecting a mixture of soils with higher sulfur abundances and bedrock with lower average sulfur abundances. King and McLennan (2010) further noted that the sulfur cycle is arguably the most important geochemical cycle on Mars. Given the ubiquitous occurrence of sulfur on terrestrial planets, it is clear that understanding interactions of sulfur gasses with basalts, the most common rock types on terrestrial bodies, is important.

This study seeks to evaluate the extent to which each of these three factors and mechanisms are viable in terrestrial rocks at Halemaumau crater at the Kilauea volcano: high sulfur solubility in primary magmas, surface-atmospheric interaction, and aqueous processing. Since March 19, 2008, there have been more than five years of renewed, continuous fumarole and volcanic activity there. Six months after that initial explosive eruption opened a 35 m wide

crater on the south wall, a roughly 158×213 m vent containing a lava lake has continued to grow. The eruptions have included significant releases of SO_2-rich gases at rates averaging 800-1200 tonnes per day (Hawaiian Volcano Observatory, 2013), with highly concentrated emissions containing up to 600 ppm SO_2 (Martin et al., 2009). Halemaumau samples collected from the area provide a natural laboratory for studying the interactions between SO_2-rich gasses and Hawaiian basalts, i.e., to test the acid fog model (e.g., Banin et al. 1997). In this model a magmatic S-HCl vapor interacts with H_2O to form an acidic solution (pH < ~2) that can then react with the basaltic components to produce an alteration assemblage. In this paper, mineralogical and geochemical effects of SO_2 weathering on basalts are evaluated through study of samples collected directly downwind and in the path of the gas plume at Halemaumau. We characterize them using electron microscopy, X-ray diffraction, and Mössbauer spectroscopy with a goal of understanding likely mineral assemblages associated with basaltic alteration under these conditions and their relevance to other planetary surfaces.

METHODS AND SAMPLES STUDIED

Bulk rock samples were obtained courtesy of staff at the Hawaii Volcano Observatory (Tim Orr, Kelly Wooten, and Maggie Mangan) from distances of 100-150m S-SE of the Halemaumau overlook in late March of 2010 (Figure 1). Samples are friable vesiculated basalts with yellowish white coatings in vesicles and in varying thicknesses upon the surface. Some samples contain fresh black basaltic material, whereas others are altered throughout, with only alteration phases evident (one sample was so altered that it was completely amorphous to XRD). The bulk composition of the unaltered igneous material in these samples is shown in Table 1 (USGS standard BHVO-1), along with representative mineral compositions from the

literature. Although the samples for this study were not collected in the exact location of BHVO-1 material for BHVO-1 was collected from a 1919 Halemaumau lava flow that is similar in both age and location to our samples making it a reasonable bulk composition.

X-Ray Diffraction (XRD)

Chunks containing both basalt and alteration material were powdered by hand. Samples were analyzed by Actlabs using a Panalytical X'Pert Pro diffractometer equipped with a Cu X-ray source. X-ray conditions included 40 kV voltage, 40 mA current, 4-80° 2θ range in 0.02° steps at 1s/step. The divergence slit was fixed at a 1° angle, the receiving slit size was 0.2 mm, and the sample was rotated at 1 rev/s.

Semi-quantitative amounts of the crystalline phases in the samples were estimated using the integrated peak intensities of the strongest peak for each mineral or the reference intensity ratio (RIR). Intensities were normalized with values of $k = I_{unknown} / I_{corundum}$, from the Powder Diffraction File (PDF) database at Actlabs. The normalization factor k for a compound is the ratio of its strongest peak intensity ($I_{unknown}$) to the intensity of the strongest peak ($I_{corundum}$) in corundum (Al_2O_3), in a sample containing 50% of the unknown and 50% corundum. Results for our samples were compared with other values of k measured and reported by different researchers, as collected in the PDF database.

Scanning Electron Microscopy (SEM) and Electron Probe Microanalysis (EPMA)

Whole samples were gold or carbon coated to allow inspection of surface alteration. Some samples were also encased in epoxy and sliced and polished to make thick sections to facilitate observation of alteration textures and compositions. Back-scatter electron (BSE) and secondary electron (SEI) images and X-ray intensity maps were collected at Tufts University using a JEOL 6300 scanning electron microscope and the Revolution software package for data

reduction. Additional X-ray intensity maps and major and minor element quantitative analyses on the altered regions were collected on the University of Massachusetts Amherst Cameca SX-50 electron probe. Altered material analyses were obtained using a 15 kV acceleration voltage, 10 nA beam current, and a defocused beam (diameter = 5–15 μm). Natural glass and mineral standards were used for calibration.

Mössbauer Spectroscopy

Approximately 10-30 mg of each sample were mixed with sugar under acetone before mounting in a sample holder confined by Kapton® polyimide film tape. Mössbauer spectra were acquired using a source of ~60 mCi ^{57}Co in Rh on a WEB Research Co. model WT302 spectrometer (Mount Holyoke College) at 295K. Results were calibrated against a 25 μm α-Fe foil. Spectra were collected in 2048 channels and corrected for nonlinearity via interpolation to a linear velocity scale defined by the spectrum of the 25 μm Fe foil used for calibration. Data were then folded before fitting, using the WMOSS Auto-fold procedure that folds the spectrum about the channel value that produces the minimum least squares sum difference between the first half of the spectrum and the reflected second half of the spectrum.

For each sample, the fraction of the baseline due to the Compton scattering of 122 keV gammas by electrons inside the detector was determined, and all spectra were then corrected to allow accurate determination of % absorption in the spectra. Run times were 6-24 hours per spectrum, with baseline counts ~2-4 million after the Compton correction.

Spectra were fit with doublets and sextets using the MEX_FielDD program acquired from the University of Ghent courtesy of E. DeGrave. Center shifts (CS, or δ), and quadrupole splittings (QS, or Δ) of the doublets were allowed to vary, and widths (full width at half maximum) of all four peaks were coupled to vary in pairs. Errors on center shift and quadrupole

splitting of well-resolved peaks are usually ±0.02 mm/s in natural samples (e.g., Skogby et al. 1992). Reproducibility (precision) of peak areas based on repeated fits using different constraints (δ, Δ, width, and areas constrained in all possible combinations of individual peaks and pairs) and fitting models (Lorentzian, Gaussian, quadrupole splitting distributions) is ±0.3% absolute for these well-resolved spectra; accuracy has been determined in previous studies of amphiboles to be ±3-5% (Dyar, 1989). For absolute site occupancy measurements based on peak areas, saturation corrections and recoil-free fraction effects may be considered, but samples in this study were prepared as thin absorbers and proper values of *f* for these mixed phases were not known, so the areas were not corrected. However, in this study, the emphasis is on constraining phase identification rather than on accurately determining phase abundances, so even peak area errors of ±3-5% would be acceptable.

RESULTS

XRD Results

XRD results from the six samples analyzed are shown in Table 2. Basalt components (pyroxene and plagioclase) are still present in some samples, but all samples show significant alteration to mostly sulfates. Two samples contain small amounts of anatase, which is likely an alteration product of the primary igneous Fe-Ti oxides (Table 1). Cristobalite was found in sample H10-7; it could be either primary (as the end-product of high temperature, lower pressure crystallization) or secondary (formed by either vapor phase deposition or devitrification of volcanic glass). The remaining phases are all sulfate alteration products: gypsum ($CaSO_4 \cdot 2H_2O$), anyhydrite ($CaSO_4$), and natroalunite ($NaAl_3(SO_4)_2(OH)_6$). No phyllosilicates were observed,

suggesting that either the fluid reaction with the rock was not complete (Schiffman et al. 2006) or that there was kinetic suppression of crystalline aluminosilicate phases (McCollom et al. 2013).

SEM and EPMA Results

SEM EDS observations are consistent with the XRD data, and show the sulfates forming as euhedral to subhedral grains with ~1 μm diameters on the rock surface and lining vesicles (Figures 2, 3). The pristine basalt phase assemblage varies among samples; augite and plagioclase are the majority phenocryst phases in all samples with glass and FeTi oxides present in varying amounts (Figure 4A). Glass appears both pristine and partially altered in the samples containing the phase. Multiple generations of alteration are observed in the X-ray intensity maps. The fresh basaltic interior is rimmed with a 10-100 μm thick layer of amorphous silica, often showing multiple layers (Figures 3, 4D). Following the amorphous silica, the outermost surface is rimmed with a patchy, 10-150 μm thick layer of sulfate material (Figures 3, 4D). Both Si-rich and S-rich rims are irregular in shape and preserve sharp boundaries between different compositional layers. The sulfate rim is rarely a continuous layer (Figure 2) and often appears thickest in surface depressions or vesicles. The presence of multi-layered rims is similar to those reported by Bishop et al. (2007) in basaltic tephras from Haleakala that were subjected to alteration near cinder cone vents.

X-ray intensity maps also indicate that silicate glass, plagioclase, augite, and FeTi oxides (when present) are all extensively reacted. BSE images show feathery amorphous silica replacing glass, with projections of the alteration phase often following cracks in the sample (Figures 4B, C). This results in a patchwork appearance of unaltered glass surrounded by amorphous silica reaction product. In addition, where plagioclase or augite phenocrysts are near the alteration

surface, replacement of these phases, often pseudomorphic, with amorphous silica is observed (Figures 4C, E, F). FeTi oxide grains, when observed, are altered to anatase.

Mössbauer Results

Mössbauer spectra of all the basalts show a range of features corresponding to Fe^{3+} in jarosite/alunite group minerals and pyroxene, Fe^{2+} in pyroxene, olivine, and ilmenite, and both Fe^{2+} and Fe^{3+} in Fe oxides (Table 3; Figures 5 and 6). Although jarosite and alunite cannot be identified solely on the basis of their Mössbauer parameters because they are so similar to several other Fe^{3+} sulfates (Dyar et al. 2006), the other XRD data in this study constrains the assignment of the Fe^{3+} doublets to primarily those of jarosite (the common Fe^{3+}-bearing alunite group mineral species). The same parameters would likely to be found anywhere along the solid solution between alunite and jarosite. Note that is this work we are fitting two different doublets to the alunite group minerals, one with $\Delta = 0.7$ mm/s and one ca. 1.3 mm/s, in keeping with the extensive studies of jarosite by Rothstein (2006) and Dyar et al. (2006). In addition, some percentage of the Fe in naturally-occurring clinopyroxenes is generally Fe^{3+} with parameters (McGuire et al. 1991) similar to those found for lower Δ doublet in the alunite group, so some of the Fe^{3+} may also be in pyroxene. All the Fe^{2+} doublets in these spectra likely represent Fe in pyroxene or olivine. The doublets with quadrupole splitting (QS) values from 1.94-2.14 mm/s represent Fe^{2+} in the M2 site (Dyar et al. 2013). The other Fe^{2+} doublet, with higher quadrupole splitting of 2.58-2.73 mm/s, is probably some combination of superimposed $^{[M1]}Fe^{2+}$ pyroxene doublets (for which QS typically ranges from ~2.5-2.7 mm/s) and olivine (QS = 2.8-3.1 mm/s; Dyar et al. 1989).

At least one Fe oxide phase is present in all samples except the exterior of H10-9. An Fe^{2+} doublet with the diagnostic parameters of ilmenite is seen as a small proportion of the total

Fe in samples H10-2, H10-8, and H10-9 (interior). In H10-2, H10-4 (both exterior and interior samples), and H10-7, Mössbauer spectra include a pair of prominent sextets with parameters that unequivocally identify the represented phase as magnetite. Samples H10-6 and H10-9 (interior) also contain sextets characteristic of magnetic phases (Figure 5), but the sextets are so small that independent evidence is needed to constrain their assignment.

Such evidence is found in the petrographic literature on Kilauean basalts, where Fe oxides have been studied carefully. The oxygen fugacity of Hawaiian basalts from Kilauea was originally suggested to be close to the fayalite-magnetite-quartz (FMQ) buffer based on in situ measureemnts (Fudali 1965, Sato and Wright 1966, Peck and Wright 1996) or alternatively, slightly above FMQ (Wright and Weiblen 1968) or closer to nickel-nickel-oxide (Helz and Thornber 1987) based on the Buddington and Lindsley (1964) geobarometer. For example, Anderson and Wright (1972) studied three fractionated lavas from Kilauea and observed coexisting magnetite and ilmenite phenocrysts from which they calculated initial crystallization of Fe and Ti oxides to a relatively cool magma (ca. 1050-1180 °C) with f_{O2} = -10.2 to -7.7. However, more modern measurements (Rhodes and Vollinger 2005) have shown that the initial oxygen fugacity of Hawaiian parent magmas is closer to magnetite-wustite. In any case, these studies suggest that the fugacity of primitive lavas forming the ejecta of the recent Halemaumau eruptions are far from oxidizing enough to contain hematite or other solely Fe^{3+} oxides, so these petrologic studies thus constrain the assignment of the poorly-resolved Fe oxide sextets observed in samples H10-6 and H10-9 (interior).

Although 8-33% of the total Fe in these samples is in these oxide phases, these percentages do not imply that oxides are present in these rocks at such high modal abundances because the other phases present do not contain as much total Fe. For example, if the sulfate

phase in these rocks is natroalunite as identified by XRD, then it clearly has a small amount of alunite group solid solution introducing Fe^{3+} into its structure, an observation confirmed through EDS element mapping. Consider then that a unit cell of alunite, with a volume of 731 $Å^3$ for four formula units of $KAl_3(SO_4)_2(OH)_6$, contains 12 Al cations. If one-fourth of the Al is substituted by Fe^{3+}, then that yields 0.4 Fe^{3+} cations per 100 $Å^3$ volume. Magnetite (Fe_3O_4, with a unit cell 591 $Å^3$ volume for eight formula units) would contain ~4.0 Fe^{3+} cations per 100 $Å^3$ volume. Thus a hypothetical sample with equal amounts of alunite and magnetite by volume would have a Mössbauer spectrum in which magnetite peaks had 10 times the area of those from the alunite group. As a result of this line of reasoning, we can conclude that magnetite is present in most of these samples, but at very low levels, ca. 1-3% by volume, that may not be detected by microanalysis.

DISCUSSION

Modeled Mineralogy

The observed alteration mineralogy is consistent with the assemblage predicted by Treiman and Schwenzer (2009), who simulated basalt weathering using SUPCRT, Thermocalc, and associated databases; these predicted the presence of anhydrite, plagioclase, pyroxene, quartz, cordierite, and hematite (see reactions below: Zolotov et al. 1997, Treiman and Schwenzer 2009). The phase assemblage is also identical to that observed in acid-sulfate basalt alteration experiments reported by McCollom et al. (2013); the phases observed over a range of heating intervals and initial fluid:rock ratios were amorphous silica, anhydrite, natroalunite, and minor FeOx.

The work of Schiffman et al. (2006) shows the effects of acid fog deposition at Kilauea prior to the recent increases in gas output; they documented the presence of an alunite group sulfate (jarosite) and amorphous silica rock coatings. They also reported the presence of a Ca-sulfate mineral as a minor constituent. Additionally, Mössbauer spectroscopy of those samples indicated the presence of minor amounts of hematite. The models of Schiffman et al. (2006) suggest that at very low effective rock to-water ratios, basaltic glass dissolution takes place, followed by evaporative precipitation of alteration phases in the order: amorphous silica, jarosite, gypsum.

Interpretation of Mössbauer results

Although the combination of Mössbauer and XRD does an excellent job of identifying the phases present in these rocks and their approximate abundances (at least with respect to the distribution of Fe cations), the relative amounts of these phases in each of the samples studied here also provide information about the changing oxidation state as acid weathering progresses. For example, the lack of ilmenite or magnetite in the exterior of H10-9 suggests that when the sulfate weathering reaction proceeds, the Fe oxide is removed even before the breakdown of pyroxene or olivine.

One important reaction is the conversion of Fe^{2+} in pyroxene (suggested to be augite by XRD) to Fe^{3+} in natroalunite (i.e., partial solid solution with the Fe^{3+}-bearing alunite species jarosite). In both samples for which pairs of interior and exterior rock were sampled, the Fe^{2+}(pyroxene) > Fe^{3+}(alunite group mineral) in the interior, and the reverse for exterior samples (Figure 5). Meanwhile, the oxides are also breaking down. There are only two samples with no Fe oxide: H10-8 and the exterior of H10-9. If we assume that the starting basalt composition of

these rocks was the same in all cases, then the eight samples here represent a progression in acid-sulfate alteration: from the least altered rock with the highest amount of Fe in oxides (H10-2), to H10-4 (interior), H10-4 (exterior), H10-7, H10-9 (interior), H10-6, H10-8, and H10-9, the most completely altered of the samples studied. However, even the most pristine sample (H10-2) still contains alunite group minerals, so even at several cm depth into the rock, acid sulfate weathering has begun to break down the rock, even while both ilmenite and magnetite are stable.

This progression does not necessarily match the phase abundances determined by XRD, where the relative proportions of phases also suggest varying degrees of acid sulfur weathering in the bulk rocks. Our XRD results indicate that sample H10-2, which is composed entirely of X-ray amorphous material (likely amorphous silica) is the *most* altered rock, followed by H10-7, in which all the primary silicates have reacted away. XRD results then suggest that H10-6, which lacks plagioclase and has only a small amount of augite remaining, has experienced extensive alteration. H10-4, H10-8, and H10-9 all retain the two primary phases (pyroxene and plagioclase) though gypsum has begun to form in all of them.

The apparent contrast between the XRD results and those from Mössbauer arises for several reasons. First of all, the original samples were highly hetrogeneous (some were simply clumps of rubble), and because the exact same samples could not be used for both analyses, it is possible that different splits contained varying mineralogy. Second, XRD is using bulk samples, mixing interior and exterior mineralogy, while the Mossbauer splits were specifically sampled to obtain contrasting results from the interior and exterios of specific samples. Third, Mössbauer is "seeing" only the distribution of Fe atoms, not the phase percentages that are measured by XRD. On the other hand, XRD does not "see" amorpous phases, which clearly constitute a significant modal percentage of some of these rocks. Finally, multiple reaction pathways are viable here. The

mobility of Fe species recorded by Mössbauer spectroscopy is the result of oxidation reactions (i.e., King and McSween 2005). The changes in bulk mineralogy measured by XRD are likely resulting from fluid rock reactions (i.e., Tosca et al. 2004, Golden et al. 2005). These different, likely concurrent, reaction pathways may result in the dissimilar alteration mineralogy progression observed in the Halemaumau samples using XRD versus Mössbauer data. However, what is clear is that Fe oxides act as proxies that identify relatively unaltered rocks, and that the acid sulfate weathering reactions are redistributing the Fe out of the oxide phases into the fluid at the same time as Fe in pyroxenes is being oxidized to form sulfate minerals, in this case alunite.

Mass Balance

A comparison of the bulk chemistry of the pristine basaltic material to that measured in the amorphous silica rims indicates extensive mobilization of cations occurred during alteration resulting in significant precipitation of secondary phases and minerals (Table 1). To evaluate potential losses or gains, an enrichment factor (EF) for each element was calculated following the method of Duce et al. (1975):

$$EF_i = (X_i/R)_{sample}/(X_i/R)_{fresh\ rock}$$

where X_i = concentration of element I and R = concentration of a reference element. The reference element used for normalization was K as K_2O was one of the least mobile elements in the Halemaumau basalts due to the resistance of the glass to alteration.

Overall, under the acidic conditions prevalent at Halemaumau, Ca, Mg, Fe, Na, and Al were almost totally leached from the glass with alteration progressing on exposed surfaces and along cracks leaving behind only residual Si (Figures 4B, C, 7). The mobile elements, with the exception of Mg, which appears to have been removed from the system, were precipitated mainly

342 at the surface as the measured reaction phase assemblage gypsum + anhydrite + natroalunite. The
343 alteration/reprecipitation process described is likely responsible for the silica-sulfate layers
344 observed at Halemaumau (Figure 3). The leaching results in interior layers of residual amorphous
345 silica rimmed with surface sulfate precipitates formed as the mobile elements migrate to the
346 surface and react with atmospheric S. Therefore, precipitation of the amorphous silica appears to
347 precede that of the sulfate phases similar to that reported by Schiffman et al. (2006).
348 The bulk of the glass has been replaced by a hydrous amorphous silica phase (Table 1)
349 which is enriched in S (Figure 7). These alteration pathways are comparable to those reported in
350 other acidic volcanic settings (e.g., Africano and Bernard 2000; Markússon and Stefánsson 2011).
351 Unaltered glass was observed near partially or totally altered phenocrysts (Figures 4E, F)
352 consistent with the order of silicate dissolution under acidic conditions proposed by Rowe and
353 Brantley (1993): pyroxene > plagioclase > glass, although the presence of partially devitrified
354 glass may affect the dissolution order. This reaction order is in contrast to some laboratory
355 experiments in which glass dissolution is observed to be much faster than mineral dissolution
356 (e.g., Brantley 2008), but in agreement with more recent experiments that suggest that glass
357 dissolution rates are slower than those of minerals (McCollom et al. 2013). It is possible that
358 compositional differences among the sampled glasses, both natural and experimental, played a
359 role in the observed dissolution rate differences (e.g., Wolff-Boenisch et al. 2004).
360 Plagioclase alteration is evident as almost total leaching of Ca, Al, and Na from the grains
361 resulting in replacement with amorphous silica (Figure 4C). SEM EDS results indicate that
362 leaching takes place in the order Ca > Na > Al similar to that reported in other acidic volcanic
363 settings (Spilde et al. 1993; Africano and Bernard 2000). Ca leached from the plagioclase is
364 precipitated as gypsum or anhydrite in voids within the sample; Na and Al are likely transported

in solution to the sample surface to be precipitated as natroalunite. Amorphous silica that is pseudomorphically replacing the plagioclase appears slightly darker in BSE than the amorphous silica rims (Figure 4C). SEM EDS results suggest that the plagioclase alteration is pure Si, consistent with the alteration mechanism simply being leaching of all other cations with the exception of Si, rather than this being a Si addition process. The slightly BSE brighter rims are the result of fine-grained amorphous silica that often contains a small amount of S.

Augite phenocrysts are also extensively altered to amorphous silica from the outer edges of the grains inward (Figures 4E, F). This suggests that, similar to that observed in plagioclase, an almost total leaching of cations is occurring (Spilde et al. 1993). Leached Fe (see Mössbauer results section) and Al are transported to the sample surface and precipitate as natroalunite-jarosite and leached Ca occurs as gypsum or anhydrite precipitates. The lack of any Mg-rich alteration products, such as Mg-sulfates or phyllosilicates, suggests that the solubility of Mg-sulfate salts is high in the reacting solutions inhibiting precipitation (McCollom et al. 2013). Fe leaching is also observed in the FeTi oxides and results in replacement of ilmenite with anatase.

Relevance to Other Hawaiian Localities

Several previous studies are relevant to this work because they also deal with alteration of Hawaiian basalts. Morris et al. (1996, 2005) studied yellow tephra from a cone on the summit of Mauna Kea, and demonstrated the presences of K-rich jarosite by XRD, in contrast with the work of Wolfe et al. (1996) who reported alunite. Morris et al. (1996) reported an assemblage that included smectite, quartz, kaolinite, gypsum, mica, and plagioclase feldspars in various samples. Bishop et al. (2007) studied alteration of samples from Haleakala volcano and reported the presence of Fe oxides, phyllosilicates, and sulfates forming from alteration of feldspar, glass, pyroxene, and olivine. Schiffman et al. (2006) report the mineralogy of coatings from acid fog

deposits at Kileaua and reported the presence of amorphous silica, gypsum, jarosite and ferrihydrite, similar to those observed here but without pyroxene. The alteration assemblages observed in this study likely reflect different starting compositions, water:rock ratios, oxidation environments, pH, and alteration fluid chemistry, as well as longer durations of alteration relative to those seen in the current study. The absence of goethite, hematite, and phyllosilicate minerals in the Halemaumau samples is notable as these phases have been detected in several other Hawaiian localities (Morris et al. 1996, 2005, Bishop et al. 2007). Geochemical models of acid sulfate alteration of basalts from both Hawaii (Schiffman et al. 2006) and Cerro Negro (McCollom et al. 2013) must manually suppress these phases to generate the correct alteration assemblage suggesting some sort of kinetic inhibition to precipitation of crystalline aluminosilicates and Al- and Fe-oxides/hydroxides.

Relevance to the Surface of Mars

Sulfate-rich outcrops and rocks have been identified at multiple locations on the martian surface both by landers and orbiters (e.g., Squyres et al. 2004, Bibring et al. 2005, 2006, Gendrin et al. 2005, Murchie et al. 2007, Murchie et al. 2009). The mineralogy of these deposits inferred from spectral measurements include kieserite, gypsum, szomolnokite, epsomite, and members of the alunite mineral group (e.g., Klingelhöfer et al. 2004, Bibring et al. 2005, 2006, Murchie et al. 2007, Bishop et al. 2009). In particular, the MIMOS II Mössbauer instrument on the MER's showed a mixture of alunite group minerals, hematite, and basalt at Meridiani Planum and a range of mineralogies at Gusev Crater including silicates (olivine and pyroxene), Fe^{3+} sulfate, ilmenite, magnetite, goethite, and nano-phase oxide (Klingelhöfer et al. 2006).

Several mechanisms have been proposed for sulfate formation on Mars and the mineralogy of the sulfate depends primarily on fluid composition, pH, temperature, and oxidative

411 environment (e.g., King and McSween 2005). Mechanisms include acidic weathering at low
412 fluid/rock ratios (Tosca et al. 2005, Hurowitz et al. 2006), acidic weathering with variable
413 oxidation state (King and McSween 2005, Tosca et al. 2008), and weathering at neutral pH (King
414 et al. 2004). Each method results in different sulfate mineralogy, crystallization sequence, and
415 other alteration phases (for a detailed review of these methods see King and McLennan 2010).
416 For example, the low fluid/rock ratio acid-sulfate model results in amorphous silica production
417 and suppression of phyllosilicates. Acid-sulfate alteration of volcanic material, either through
418 hydrothermal methods (McCollom and Hynek 2005) or in the gas phase ("acid fog" Tosca et al.
419 2004, Schiffman et al. 2006, Zolotov and Mironenko 2007), has been shown to be both
420 geologically and geochemically feasible as a mechanism for producing martian sulfate-rich
421 deposits, although all of the above mechanisms may be applicable to certain regions on Mars.
422 Widespread martian volcanism would provide a direct source for the SO_2 gas required for acid
423 sulfate alteration as well as a small amount of H_2O degassing from the magmas.
424 The magmatic and alteration assemblages observed at Halemaumau, plagioclase,
425 pyroxene, ilmenite, magnetite, and sulfate, and the lack of phyllosilicates, are similar to those
426 recorded by the MERs, indicating that Halemaumau may be a good terrestrial analogue for some
427 martian alteration pathways. Hematite and goethite are noticeably absent at this terrestrial
428 locality. In addition, geochemical modeling of acid sulfate alteration of Gusev derived basalts by
429 Berger et al. (2009) and McCollom et al. (2013), Adirondack and Barnhill class, respectively,
430 predict similar alteration assemblages to those observed at Halemaumau. The modeled phases
431 include amorphous silica, anhydrite, natroalunite, and kieserite (McCollom et al. 2013) or
432 chalcedony, jarosite, gypsum, epsomite, and goethite (Berger et al. 2009). Both modeled

433 assemblages are similar to those observed in this study and suggest that acid fog alteration, like
434 that currently operating at Halemaumau, is a strong candidate for alteration mechanisms on Mars.
435
436 **Relevance to the Surface of Venus**
437 Due to the high sulfur content of the Venusian atmosphere, alteration products high in
438 sulfates are to be expected. However, all terrestrial basalt weathering reactions occur in the
439 presence of water at a slow rate (relative to 93 bar, 740K conditions on Venus). Although there
440 are small amounts of H_2O remaining in the Venusian atmosphere, water is unlikely to play a
441 major role in Venus weathering reactions. This suggests that anhydrous reactions may be
442 favored, such as those recorded by Treiman and Schwenzer (2009):
443 diopside + atmospheric S ↔ anhydrite + enstatite + quartz
444 $CaMgSi_2O_6 + SO_3 \leftrightarrow CaSO_4 + MgSiO_3 + SiO_2$ and
445 plagioclase + atmospheric S ↔ anhydrite + andalusite + quartz
446 $CaAl_2Si_2O_8 + SO_3 \leftrightarrow CaSO_4 + Al_2SiO_5 + SiO_2$
447 On Venus, carbonate alteration phases might also be prevalent, but there is no
448 terrestrial analogue that replicates those conditions.
449 If mineral assemblages like those measured in our Halemaumau samples were
450 observed on Venus, it would be possible to back-calculate a range of major element
451 abundances of the parent rock, in a manner similar to the work done (e.g., Figure 7).
452 These Halemaumau basalts thus provide a useful demonstration of how basalt alteration
453 might be driven by SO_2-rich gas.
454
455 **Implications**

456 The alteration mechanisms and phase assemblages observed at Halemaumau may
457 be good analogues for basalt alteration on other rocky planetary bodies, i.e., Mars,
458 Venus, Mercury, Io, where S is ubiquitous and low fluid/rock ratios are common. As
459 more data from these bodies is returned by current and future missions a deeper
460 understanding of the sulfur cycle on these planets is required to more completely
461 characterize their geology. Additionally, as evidenced by these samples from
462 Halemaumau, as well as samples from other volcanic localities, these alteration
463 processes are observed terrestrially in a variety of settings. Further elucidation of the
464 terrestrial sulfur cycle has implications for volcanic degassing, atmospheric chemistry,
465 and climate cycles.
466
467 **Acknowledgments:** We thank Tim Orr, Kelly Wooten, and Maggie Mangan of
468 the USGS/HVO for collecting and sharing these samples, Elitsa Hrischeva for XRD
469 analyses, and Melissa Nelms and Elly Breves for Mössbauer data processing. We also
470 acknowledge Lindy Elkins-Tanton for many helpful discussions and reviews of early
471 manuscripts. This manuscript was improved by thoughtful reviews from Weigang Kong
472 and Tom McCollom. This research was supported by NASA grant NNX11AF11G and
473 student funding from the Massachusetts Space Grant Consortium.
474
475 **REFERENCES**

476 Africano, F. and Bernard, A. (2000) Acid alteration in the fumaroles environment of the Usu
477 volcano, Hokkaido, Japan, Journal of Volcanology and Geothermal Research, 97, 475-
478 495.

Anderson, A.T., and Wright, T.L. (1972) Phenocrysts and glass inclusions and their bearing on oxidation and mixing of basaltic magmas at Kilauea volcano, Hawaii, American Mineralogist, 57, 188–216.

Banin, A., Han, F.X., Kan, I., and Cicelsky, A. (1997) Acidic volatiles and the Mars soil, Journal of Geophysical Research, 102, 13,341-13,356.

Berger, G., Toplis, M.J., Treguier, E., D'Uston, C., and Pinet, P. (2009) Evidence in favor of small amounts of ephemeral and transient water during alteration at Meridiani Planum, Mars, American Mineralogist, 94, 1279–1282.

Bibring, J.-P. et al. (2005) Mars surface diversity as revealed by the OMEGA/Mars Express observations, Science, 307, doi:10.1126/science.1109509.

Bibring, J.-P. et al. (2006) Global mineralogical and aqueous Mars history derived from OMEGA/Mars Express data, Science, 312, 400-404.

Bishop, J.L., Schiffman, P., Murad, E., Dyar, M.D., Drief, A., and Lane, M.D. (2007) Characterization of alteration products in tephra from Haleakala, Maui: A visible-infrared spectroscopy, Mossbauer spectroscopy, XRD, EMPA and TEM study, Clays and Clay Minerals, 55, 1-17.

Bishop, J.L., Parente, M., Weitz, C.M., Noe Dobrea, E.Z., Roach, L.H., Murchie, S.L., McGuire, P.C., McKeown, N.K., Rossi, C.M., Brown, A.J., Calvin, W.M., Milliken, R., and Mustard, J.F. (2009) Mineralogy of Juventae Chasma: Sulfates in the light-toned mounds, mafic minerals in the bedrock, and hydrated silica and hydroxylated ferric sulfate on the plateau, Mars, Journal of Geophysical Research, 110, doi:10.1029/ 2009JE003352.

Blewett, D.T., Chabot, N.L., Denevi, B.W., Ernst, C.M., Head, J.W., Izenberg, N.R., Murchie, S.L., Solomon, S.C., Nittler, L.R., McCoy, T.J., Xiao, Z., Baker, D.M.H., Fassett, C.I.,

Braden, S.E., Oberst, J., Scholten, F., Preusker, F., and Hurwitz, D.M. (2011) Hollows on Mercury: MESSENGER evidence for geologically recent volatile-related activity, Science, 333, 1856-1859.

Brantley, S.L. (2008) Kinetics of mineral dissolution. In S.L. Brantley, J.D. Kubicki, and A.F. White, Eds., Kinetics of Water-Rock Interaction, p. 151-210. Springer, New York.

Brückner, J., Dreibus, G., Rieder, R., and Wänke, H. (2003) Refined data of Alpha Proton X-ray Spectrometer analyses of soils and rocks at the Mars Pathfinder site: Implications for surface chemistry, Journal of Geophysical Research, 108, E8094, DOI: 10.1029/2003JE002060.

Buddington, A.F., and Lindsley, D.H. (1964) Iron titanium oxide minerals and synthetic equivalents, Journal of Petrology, 5, 310–357.

Clark, B.C., Baird, A.K., Weldon, R.J., Tsusaki, D.M., Schabel, L. and Candelaria, M.P. (1982) Chemical composition of martian fines, Journal of Geophysical Research, 87, 10,059-10,067.

Duce, R.A., Hoffman, G.L., Zoller, W.H. (1975) Atmospheric trace metal at remote southern and southern hemispheric sites: pollution or natural? Science 187, 59–61.

Dyar, M.D., Klima, R.E., Fleagle, A., and Peel, S.E. (in press) Fundamental Mössbauer parameters of synthetic Ca-Fe-Mg pyroxenes, American Mineralogist.

Dyar, M.D., McGuire, A.V., and Ziegler, R.D. (1989) Redox equilibria and crystal chemistry of coexisting minerals from spinel lherzolite mantle minerals, American Mineralogist, 74, 969-980.

Dyar, M.D., Podratz, L., Sklute, E.C., Rusu, C., Rothstein, Y., Tosca, N., Bishop, J.L., and Lane, M.D. (2006) Mössbauer spectroscopy of synthetic alunite group minerals, Workshop on Martian Sulfates as Recorders of Atmospheric-Fluid-Rock Interactions, Abstract #7053.

Ebel, D.S. (2011) Sulfur in extraterrestrial bodies and the deep Earth, Reviews in Mineralogy, 73, 315-336.

Fegley, B.E. Jr., and Prinn, R.G. (1989) Estimation of the rate of volcanism on Venus from reaction rate measurements, Nature 337, 55–58.

Fudali R.F. (1965) Oxygen fugacities of basaltic and andesitic magmas, Geochimica et Cosmochimica Acta, 29,1063–1075

Gellert, R., Rieder, R., Brückner, J., Clark, B.C., Dreibus, G., Klingelhöfer, G., Lugmair, G., Ming, D. W., Wänke, H., Yen, A., Zipfel, J., and Squyres, S.W. (2006) Alpha Particle X-Ray Spectrometer (APXS): Results from Gusev Crater and calibration report, Journal of Geophysical Research, 111, E02S05, DOI: 10.1029/2005JE002555.

Gendrin, A., et al. (2005) Sulfates in Martian layered terrains: The OMEGA/Mars Express view, Science, 307, doi:10.1126/science.1109087.

Golden, D.C., Ming, D.W., Morris, R.V., and Mertzman, S.A. (2005) Laboratory-simulated acid-sulfate weathering of basaltic materials: Implications for formation of sulfates at Meridiani Planum and Gusev crater, Mars, Journal of Geophysical Research, 110, doi:10.1029/2005JE002451.

Hawaiian Volcano Observatory website: http://volcanoes.usgs.gov/hvo/activity/kilaueastatus.php.

Helz, R.T., and Thornber, C.R. (1987) Geothermometry of Kilauea Iki lava lake, Hawaii, Bulletin de Volcanologie, 49, 651–668.

King, P.L. and McSween, H.Y.Jr. (2005) Effects of H_2O, pH, and oxidation state on the stability of Fe minerals on Mars, Journal of Geophysical Research, 110, doi:10.1029/2005JE002482.

King, P.L., and McLennan, S.M. (2010) Sulfur on Mars, Elements, 6, 107-112.

Klingelhöfer, G. et al. (2004) Jarosite and hematite at Meridiani Planum from Opportunity's Mössbauer spectrometer, Science, 306, 1740-1745.

Klingelhöfer, G., Morris, R.V., De Souza, P.A. Jr., Rodionov, D., and Schröder, C. (2006) Two earth years of Mössbauer studies of the surface of Mars with MIMOS II, Hyperfine Interactions, 170, 169-177.

Krasnopolsky, V.A., and Parshev, V.A. (1981) Chemical composition of the atmosphere of Venus, Nature, 292, 610-613.

Markússon, S.H. and Stefánsson, A. (2011) Geothermal surface alteration of basalts, Krýsuvík Iceland—Alteration mineralogy, water chemistry and the effects of acid supply on the alteration process, Journal of Volcanology and Geothermal Research, 206, 46-59.

Martin, R., Ilyinskaya, E., LeBlond, J., Sawyer, G.M., Tsanev, V.I., Mather, T.A., Pyle, D.M., Sutton, A.J., Elias, T., Werner, C.A., Oppenheimer, C., and Edmonds, M. (2009) Understanding the origin of micron-sized silicate spherules emitted during quiescent degassing from the 2008-2009 summit eruption at Kilauea Volcano, Hawai'i, Eos Transactions AGU, 90(52), Fall Meet. Supplement, Abstract V43G-2332.

McCollom, T.M., and Hynek, B.M. (2005) A volcanic environment for bedrock diagenesis at Meridiani Planum, Mars, Nature, 438, 1129-1131.

McCollom, T.M., Robbins, M., Moskowitz, B., Berquó, T.S., Jöns, N., and Hynek, B.M. (2013) Experimental study of acid-sulfate alteration of basalt and implications for sulfate deposits on Mars, Journal of Geophysical Research, 118, doi:10.1002/jgre.20044.

McGuire, A.V., Dyar, M.D., and Ward, K.W. (1989) Neglected Fe^{3+}/Fe^{2+} ratios: a study of Fe^{3+} contents of megacrysts from alkali basalts, Geology, 17, 687-689.

McLennan, S.M., Boynton, W.V., Karunatillake, S., Hahn, B. C., and Taylor, G. J. (2010) Mars Odyssey GRS Team, Distribution of sulfur on the surface of Mars determined by the 2001 Mars Odyssey Gamma Ray Spectrometer, Lunar and Planetary Science Conference, Houston, TX, Abstract #2174.

Morris, R.V., Ming, D.W., Golden, D.C., and Bell, J. F. III (1996) An occurrence of jarositic tephra on Mauna Kea, Hawaii: Implications for the ferric mineralogy of the Martian surface, in Mineral Spectroscopy: A Tribute to Roger G. Burns, edited by M. D. Dyar, C. McCammon, and M. W. Schaefer, pp. 327-336, Geochemical Soc., Houston, TX.

Morris, R.V., Ming, D.W., Graff, T.G., Arvidson, R.E., Bell, J.F. III, Squyres, S.W., Mertzman, S.A., Gruener, J.E., Golden, D.C., Le, L., and Robinson, G.A. ((2005) Hematite spherules in basaltic tephra altered under aqueous, acid-sulfate conditions on Mauna Kea volcano, Hawaii: Possible clues for the occurrence of hematite-rich spherules in the Burns formation at Meridiani Planum, Mars. Earth and Planetary Science Letters, 240, 168-178.

Murchie, S. et al. (2007) Compact Reconnaissance Imaging Spectrometer for Mars (CRISM) on Mars Reconnaissance Orbiter (MRO), Journal of Geophysical Research, 112, doi:10.1029/2006JE002682.

Murchie, S., Roach, L., Seelos, F., Milliken, R., Mustard, J., Arvidson, R., Wiseman, S., Andrews-Hanna, J., Bishop, J., Bibring, J-P., Parente, M., and Morris, R. (2009) Evidence for the origin of layered deposits in Candor Chasma, Mars, from mineral

composition and hydrologic modeling, Journal of Geophysical Research, 114, doi:10.1029/2009JE003343.

Nittler, L.R., Starr, R.D., Weider, S.Z., McCoy, T.J., Boynton, W.V., Ebel, D.S., Ernst, C.M., Evans, L.G., Goldsten J.O., Hamara, D.K., Lawrence, D.J., McNutt, R.L. Jr., Schlemm, C.E., Solomon, S.C. and Sprague, A.L. (2011) The major-element composition of Mercury's surface from MESSENGER X-ray spectrometry, Science, 333, 1847-1850.

Peck, D.L., and Wright, T.L. (1966) Experimental studies of molten basalts in situ: a summary of physical and chemical measurements on recent lava lakes of Kilauea volcano, Hawaii, Geological Society of America Annual Meeting, 101, 158.

Rhodes, J.M., and Vollinger, M.J. (2005) Ferric/ferrous ratios in 1984 Mauna Loa lavas: a contribution to understanding the oxidation state of Hawaiian lava, Contributions to Mineralogy and Petrology, 149, 666-674.

Rieder, R., Gellert, R., Anderson, R.C., Brückner, J., Clark, B.C., Dreibus, G., Economou, T., Klingelhöfer, G., Lugmair, G.W., Ming, D.W., Squyres, S.W., d'Uston, C., Wänke, H., Yen, A., and Zipfel, J. (2004) Chemistry of rocks and soils at Meridiani Planum from the alpha particle X-ray spectrometer, Science, 306, 1746-1749.

Rothstein, Y. (2006) Spectroscopy of jarosite and implications for the mineralogy of Mars. B.A. thesis, Mount Holyoke College.

Rowe, G.L., Jr. and Brantley, S.L. (1993) Estimation of the dissolution rates of andesitic glass, plagioclase and pyroxene in a flank aquifer of Poás Volcano, Costa Rica, Chemical Geology, 105, 71-87.

Sato, M., and Wright, T.L. (1966) Oxygen fugacities measured directly in volcanic gases, Science, 153, 1103–1105.

614 Schiffman P., Zierenberg, R., Marks, N., Bishop, J.L., and Dyar, M.D. (2006) Acid fog
615 deposition at Kilauea volcano: A possible mechanism for the formation of siliceous-
616 sulfate rock coatings on Mars, Geology, 34, 921-924.
617 Spilde, M.N., Brearley, A.J., and Papike, J.J. (1993) Alteration of plagioclase and pyroxene
618 phenocrysts in a fissure fumarole, Valley of Ten Thousand Smokes, Alaska, American
619 Mineralogist, 78, 1066-1081.
620 Squyres, S.W. et al. (2004) In situ evidence for an ancient aqueous environment at Meridiani
621 Planum, Mars, Science, 306, 1709-1714.
622 Tosca, N.J., McLennan, S.M., Lindsley, D.H., and Schoonen, M.A.A. (2004) Acid-sulfate
623 weathering of synthetic Martian basalt: The acid fog model revisited, Journal of
624 Geophysical Research, 109, doi:10.1029/2003JE002218.
625 Tosca, N.J., Knoll, A.H., and McLennan, S.M. (2005) Geochemical modeling of evaporation
626 processes on Mars: Insight from the sedimentary record at Meridiani Planum, Earth and
627 Planetary Science Letters, 240, 122-148.
628 Tosca, N.J., McLennan, S.M., Dyar, M.D., Sklute, E.C., and Michel, F.M. (2008) Fe oxidation
629 processes at Meridiani Planum and implications for secondary Fe mineralogy on Mars,
630 Journal of Geophysical Research, 113, doi:10.1029/2007JE003019.
631 Treiman, A. H. and Schwenzer, S. P. (2009) Venus Geochemistry: Progress, Prospects, and New
632 Missions, Lunar and Planetary Science Conference, Abstract #2011.
633 Treiman, A.H., and Bullock, M.A. (2012) Mineral reaction buffering of Venus' atmosphere: A
634 thermochemical constraint and implications for Venus-like planets, Icarus, 217, 534-541.
635 Weider, S.Z., Nittler, L.R., Starr, R.D., McCoy, T.J., Stockstill-Cahill, K.R., Byrne, P.K.,
636 Denevi, B.W., Head, J.W., and Solomon, S.C. (2012) Chemical heterogeneity on

637 Mercury's surface revealed by the MESSENGER x-ray spectrometer, Journal of
638 Geophysical Research, 117, E00L05, doi: 10.1029/2012JE004153.
639 Wolff-Boenisch D., Gislason, S.R., Oelkers, E.H., and Putnis, C.V. (2004) The dissolution rates
640 of natural glasses as a function of their composition at pH 4 and 10.6, and temperatures
641 from 35 to 74°C, Geochimica et Cosmochimica Acta, 68, 4843-4858.
642 Wright, T.L., and Weiblen, P.A. (1968) Mineral composition and paragenesis in tholeiitic basalt
643 from Makaopuhi lava lake, Hawaii, GSA Special Paper, 115, 242–243.
644 Zolotov M.Y., Fegley, B., and Lodders, K. (1997) Hydrous silicates and water on Venus, Icarus,
645 130, 475-494.
646 Zolotov, M.Y. (2007) Solid planet–atmosphere interactions. In Spohn, T. and Schubert, G., Eds.,
647 Treatise on Geophysics Planets and Moons, vol. 10, p. 349–369, Elsevier.
648 Zolotov, M.Y. and Mironenko, M.V. (2007) Timing of acid weathering on Mars: A
649 kinetic-thermodynamic assessment, Journal of Geophysical Research, 112,
650 doi:10.1029/2006JE002882.

651 Figure Captions

652

653 Figure 1. Sample location map for Halemaumau Crater. Contour elevations are given in
654 feet. The inset map shows the location of Halemaumau Crater at the summit of Kilauea in
655 Hawaii. The picture was taken in 2008 during the beginnings of the new summit eruptive
656 episode.

657

658 Figure 2. SEI images of sulfates growing on amorphous silica surface in sample H10-4.
659 Sulfate phase is natroalunite. AmSil = amorphous silica.

Figure 3. SEI images and S and Si Kα element maps from sample H10-4 illustrating the S-rich rims observed on the Kilauea basalts. In addition to the S-rich outer rims, an interior amorphous Si-rich zone is present in all samples studied. (a) Box on SEI image shows locations of the S and Si element maps. (b) and (c) SEI image and element maps are at same scale. Scale bars are on all images.

Figure 4. BSE images of the reacting phases in the studied Halemaumau basalts (a-c: H10-4; d-f: H10-9). (a) Pristine basalt H10-4. (b) Extensive glass reaction to form amorphous silica. Reaction products rim the outer edge of the sample and project into unaltered glass along cracks. Arrows highlight regions of feathery amorphous silica. (c) Decomposition of plagioclase and replacement with amorphous silica. Arrows highlight regions of feathery amorphous silica. (d) Low magnification image of pristine basalt interior rimmed with amorphous silica inner rim and sulfate-rich outer rim. Division between different alteration rims and basalt denoted with white line. (e) Augite and glass within the amorphous silica rim showing extensive replacement with amorphous silica. (f) Augite and ilmenite within the amorphous silica rim showing extensive replacement with amorphous silica. Gl = glass; Plg = plagioclase; Aug = augite; AmSil = amorphous silica; FeTi = FeTi oxide.

Figure 5. Mössbauer spectra of SO_2-weathered basalts. Fe^{3+} doublets (closely-spaced peaks, orange dashed lines) represent Fe^{3+} in some combination of an alunite group mineral and pyroxene. More widely-spaced Fe^{2+} doublets represent Fe in pyroxene, and the small, bold

683 doublet is ilmenite. Magnetice sextets are shown in pink, and the spectral envelope (sum of all
684 fitted peaks) is a thin green line.
685
686 Figure 6. Mössbauer spectra of acid sulfate-weathered basalts in which interior and exterior
687 aliquots were studied. The original samples were irregular masses roughly 10 cm diameter. Each
688 was broken in half so that the interior could be sampled for contrast with the softer, sulfate-
689 weathered exterior. Colors and line patterns are as in Fig. 5.
690
691 Figure 7. Histogram of enrichment factors (EF) for different elements in the amorphous silica
692 rims as compared to those elements in unaltered basalt. The different colored lines each represent
693 a unique rind analysis. Calculation method described in text.
694
695

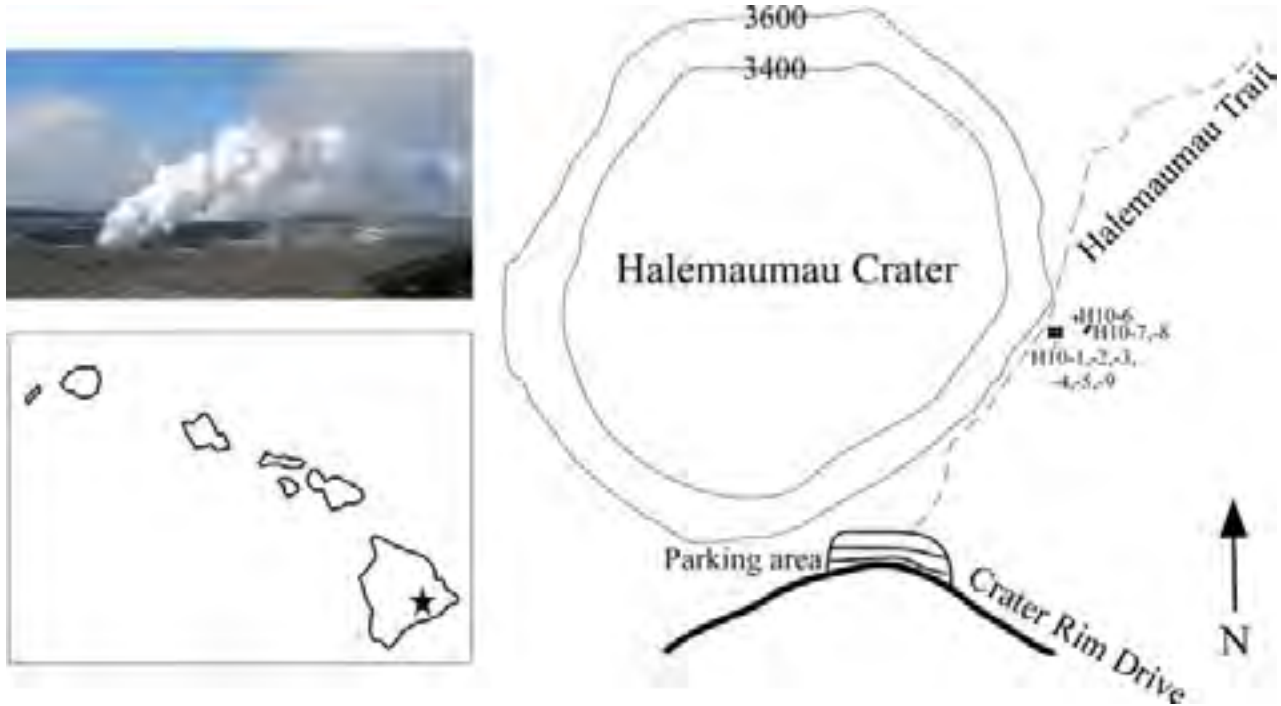
3600
3400
Halemaumau Crater
Halemaumau Trail
H10-6
H10-7,-8
H10-1,-2,-3,
-4,-5,-9
Parking area
Crater Rim Drive
N

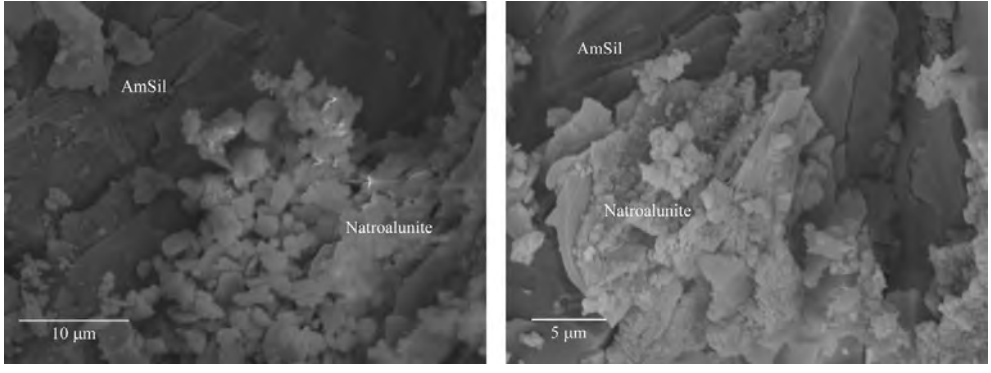
AmSil
Natroalunite
10 μm
AmSil
Natroalunite
5 μm

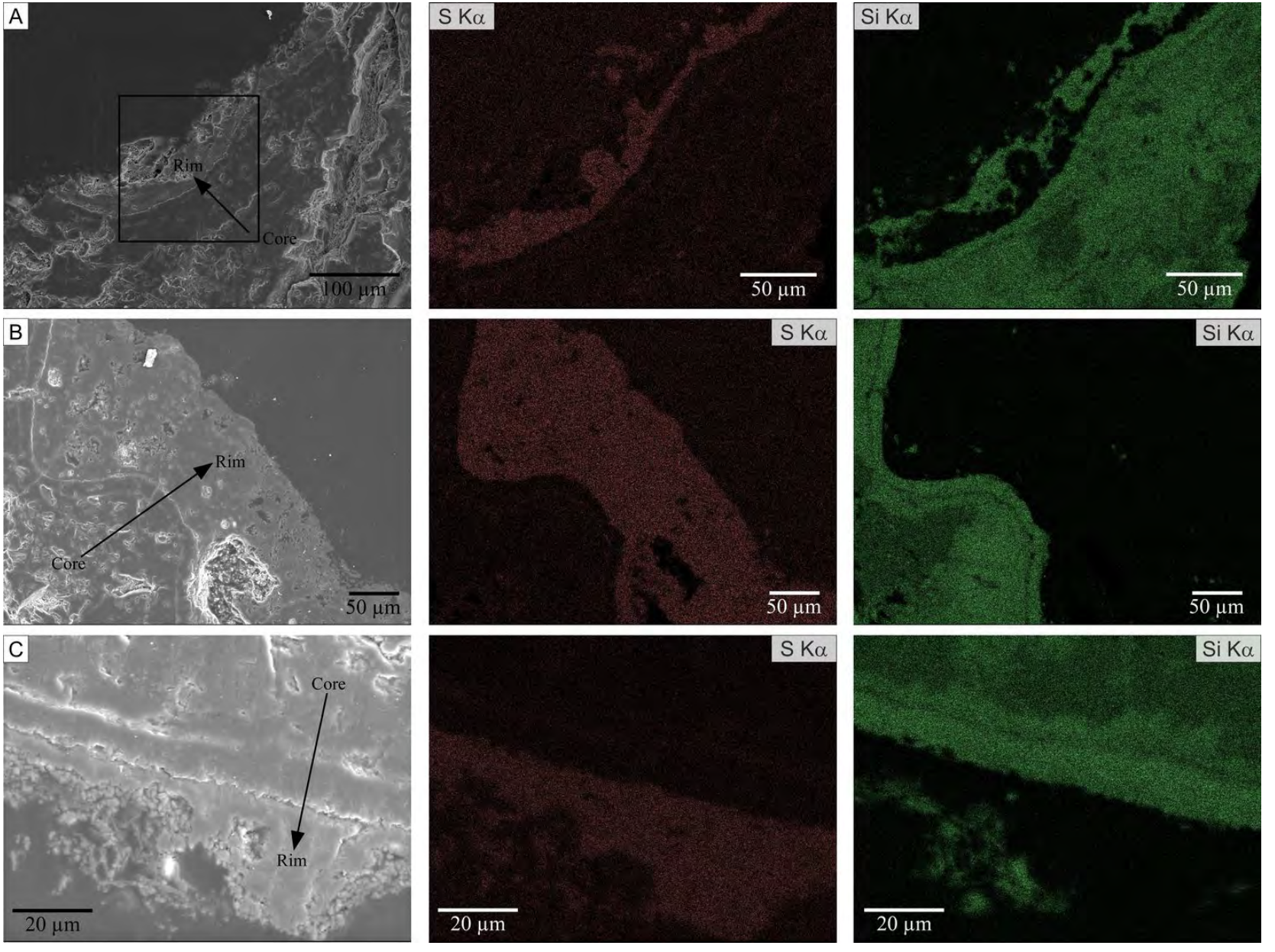
A
Rim
Core
100 µm
S Kα
50 µm
Si Kα
50 µm
B
Rim
Core
50 µm
S Kα
50 µm
Si Kα
50 µm
C
Core
Rim
20 µm
S Kα
20 µm
Si Kα
20 µm

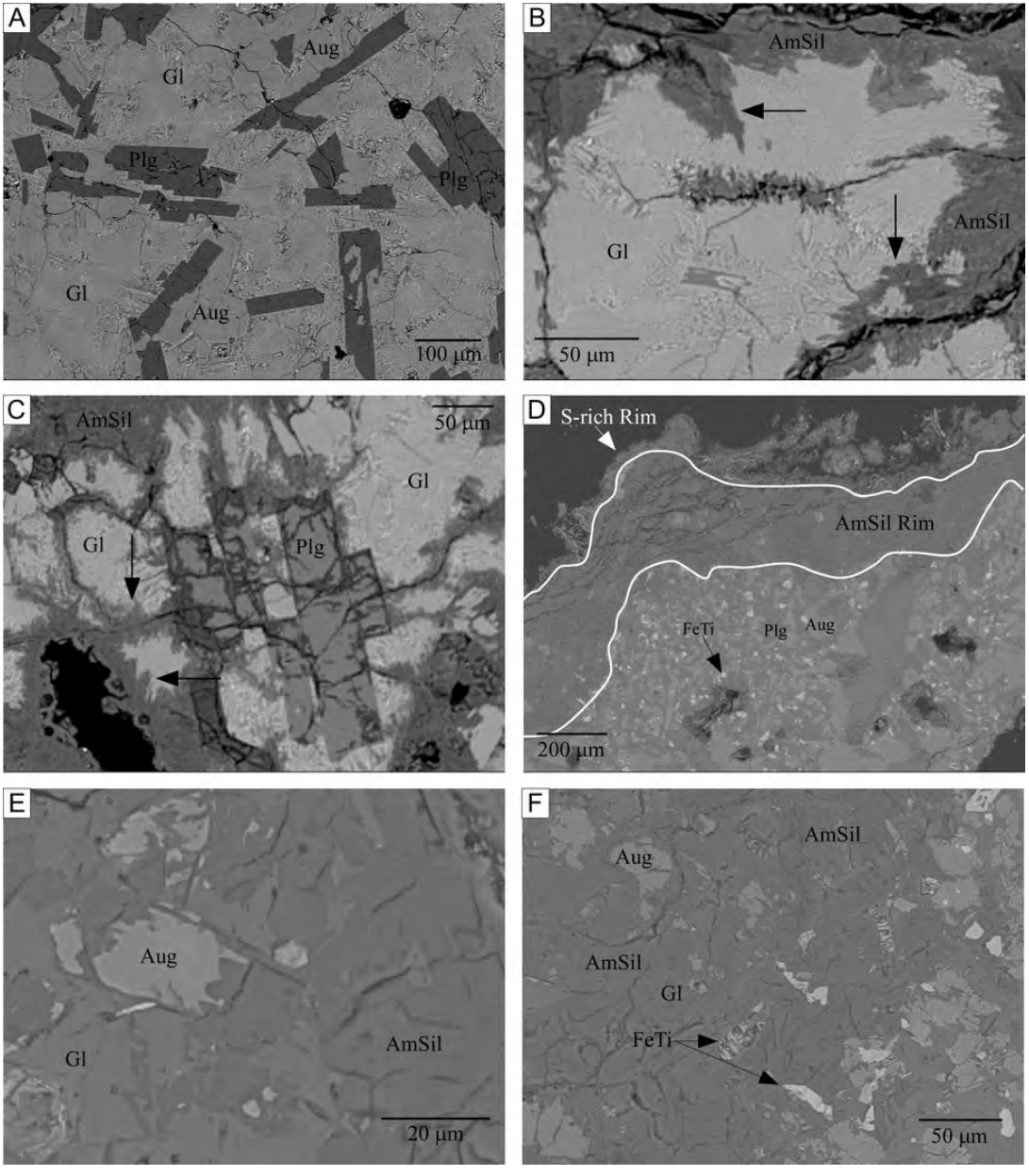
A
Aug
Gl
Plg
Plg
Gl
Aug
100 µm
B
AmSil
AmSil
Gl
50 µm
C
AmSil
50 µm
Gl
Gl
Plg
D
S-rich Rim
AmSil Rim
FeTi
Plg
Aug
200 µm
E
Aug
Gl
AmSil
20 µm
F
AmSil
Aug
AmSil
Gl
FeTi
50 µm

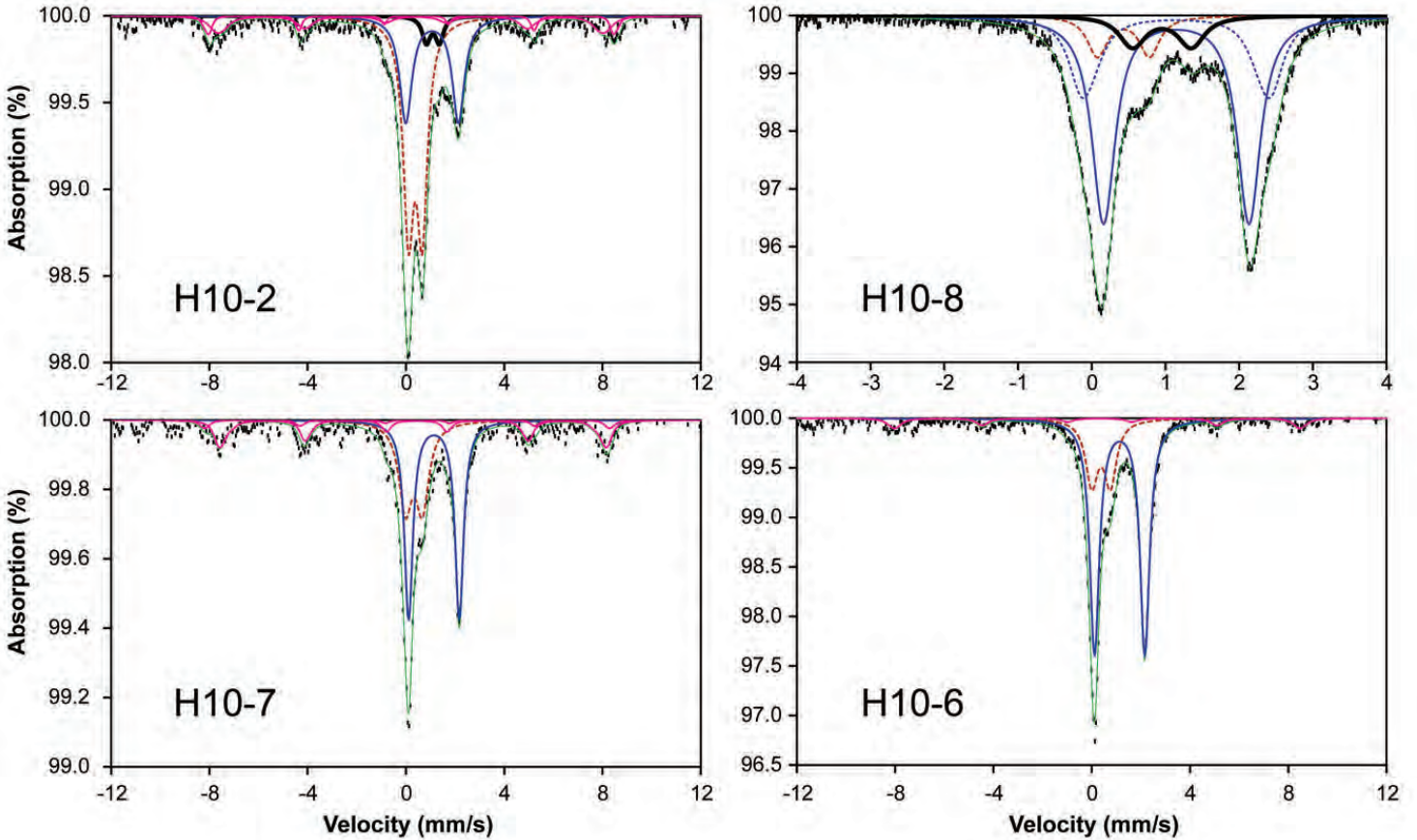
H10-2
H10-8
H10-7
H10-6
Absorption (%)
Absorption (%)
Velocity (mm/s)
Velocity (mm/s)

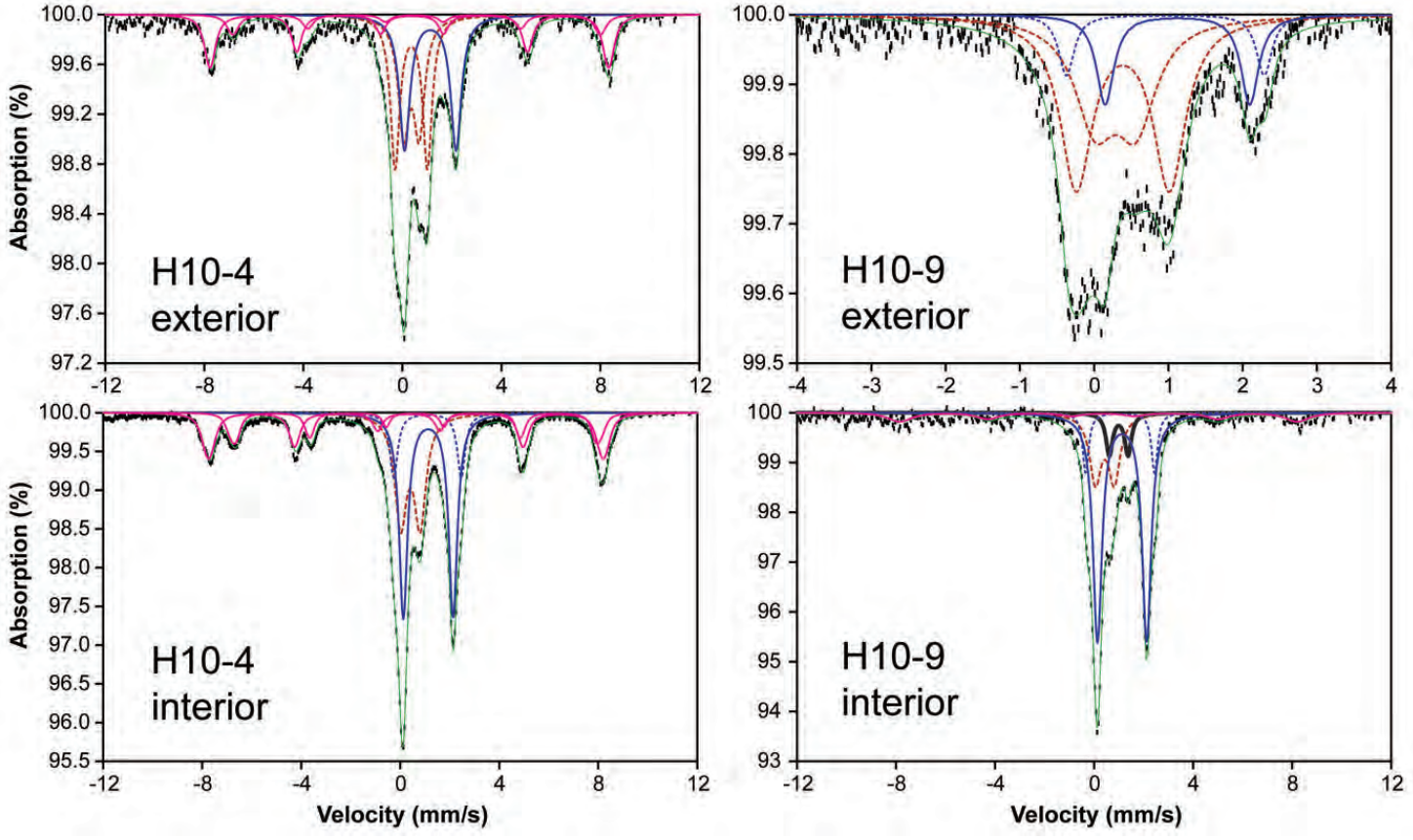
H10-4
exterior
H10-9
exterior
H10-4
interior
H10-9
interior
Absorption (%)
Absorption (%)
Velocity (mm/s)
Velocity (mm/s)

log EF
3
2
1
0
-1
-2
-3
S
SiO2
Al2O3
Nα2O
CαO
FeO
MgO
TiO2

Table 1. Unaltered bulk basalt, mineral, and rim compositions.

Oxide	BHVO-1[a]	Plagioclase[b]	Augite	Silica-rich Rim
SiO_2	49.94	52.01	50.93	89.89
TiO_2	2.71	n.m.	1.59	0.74
Al_2O_3	13.8	29.7	3.15	1.16
FeO	8.58	n.m.	9.64	0.59
Fe_2O_3	2.82	0.79	n.m.	n.m.
MgO	7.23	0.23	16.21	0.3
MnO	0.17	n.m.	0.23	0.02
CaO	11.4	14.07	18.03	0.35
Na_2O	2.26	3.48	0.23	0.15
K_2O	0.52	0.12	n.m.	0.12
P_2O_5	0.27	n.m.	n.m.	0.04
S	0.01	n.m.	n.m.	0.61
Sum	99.7	100.41	100.07	93.96

n.m. = element not measured.

[a]Bulk composition from USGS (http:/minerals.cr.usgs.go v/geo_chem_stand/basaltbhvo1.html). BHVO-1 was used as a representative bulk composition due to its collection location and age, both of which are similar to the lavas analyzed in this study. Material for BHVO-1 was collected from the surface layer of the pahoehoe lava that overflowed from Halemaumau in the fall of 1919.

[b]Mineral compositions from GeoRoc database (http://georoc.mpch-mainz.gwdg.de/georoc/Start.asp)

Table 2. Minerals Identified by XRD Analyses[a]

Sample	H10-4	H10-6	H10-7	H10-8	H10-9
Augite	34	5	n.d.	24	32
Plagioclase	45	n.d.	n.d.	16	51
Gypsum	6	72	84	56	6
Anhydrite	n.d.	23	n.d.	n.d.	n.d.
Natroalunite	15	n.d.	n.d.	n.d.	10
Cristobalite	n.d.	n.d.	10	n.d.	n.d.
Anatase	n.d.	n.d.	6	4	n.d.

n.d. = not detected.

[a]Results expressed in semi-quantitative wt%. Note that one additional sample, H10-2, was composed of 100% X-ray amorphous material.

Table 3. Mössbauer Parameters for Halemaumau Samples

Sample	Parameter	H10-2	H10-4		H10-6	H10-7	H10-9	
			Exterior	Interior			Exterior	Interior
Fe^{3+} sulfate (alunite group) or pyroxene	**CS (mm/s)**	0.38	0.36	0.41	0.38	0.32	0.29	0.44
	QS (mm/s)	0.56	0.63	0.79	0.76	0.69	0.55	0.76
	Width (mm/s)	0.52	0.54	0.58	0.6	0.65	0.66	0.57
	Area	48	22	24	24	31	34	20
Fe^{3+} sulfate (alunite group)	**CS (mm/s)**		0.36				0.39	
	QS (mm/s)		1.31				1.26	
	Width (mm/s)		0.45				0.53	
	Area		25				45	
Fe^{2+} in M1 Pyroxene and/or olivine	**CS (mm/s)**			1.1			0.98	1.1
	QS (mm/s)			2.73			2.68	2.78
	Width (mm/s)			0.39			0.25	0.3
	Area			10			8	9
Fe^{2+} in M2 pyroxene	**CS (mm/s)**	1.07	1.13	1.13	1.14	1.14	1.12	1.13
	QS (mm/s)	2.14	2.08	2.01	2.05	2.07	1.94	1.99
	Width (mm/s)	0.6	0.52	0.42	0.47	0.41	0.29	0.44
	Area	29	25	33	69	47	13	53
Fe^{2+} ilmenite	**CS (mm/s)**	1.1						0.99
	QS (mm/s)	0.53						0.76
	Width (mm/s)	0.4						0.33
	Area	5						7
$Fe^{3+}_2Fe^{2+}O_4$ magnetite	**CS (mm/s)**	0.35	0.58	0.66	0.27	0.37		0.31
	QS (mm/s)	-0.22	0.09	0.03	-0.1	-0.15		-0.18
	Field	473.3	463.3	449.4	510.1	489.1		496.8

	Width (mm/s)	0.72	0.51	0.36	0.56	0.45		1
	Area	13	8	12	8	18		10
$Fe^{3+}{}_2Fe^{2+}O_4$	**IS**	0.37	0.38	0.34		0.31		
magnetite	**QS**	-0.21	-0.11	-0.12		-0.42		
	Field	510.2	498.5	495.4		509.7		
	Width	0.25	0.49	0.48		0.4		
	Area	6	20	21		4		
	χ^2_{norm}	0.67	0.89	1.84	1.06	0.67	1.14	0.65

H10-8
0.43
0.7
0.329
1.15
2.58
0.4126
1.15
1.99
0.3755
0.97
0.8
0.49

1.23